DEPARTAMENT D'ASTRONOMIA I METEOROLOGIA

UNIVERSITAT DE BARCELONA

Near-relativistic electron events. Monte Carlo simulations of solar injection and interplanetary transport

Memòria presentada per
Neus Àgueda Costafreda
per optar al grau de Doctora
per la Universitat de Barcelona.
Barcelona, 20 de febrer de 2008

4 Modeling solar near-relativistic electron events

Modelization of SEP events aims at revealing (1) the scenario of the particle acceleration and release into interplanetary space, and (2) the properties of the subsequent particle transport through the IMF. Energetic particles released from the solar corona into interplanetary space are usually described by an injection function that contains free parameters. The particle transport along the IMF is generally described by means of a pitch-angle scattering model and the particle mean free path. Up to now, X-rays and radio solar observations have also been used to understand the scenario of particle acceleration and release (i.e. to find out where and when energetic particles are injected into interplanetary space) by a priori reducing the number of free parameters. Nevertheless, it is also possible to constrain the scenario by taking advantage of the angular information contained in the sectored time-intensity measurements at 1 AU. Then, available solar proxy observations can be used to check the outputs of the modelization.

Keeping this latter idea in mind, we have developed an algorithm that involves a simultaneous fit of the time-intensity profiles recorded by different sectors, which is applicable to the modelization of solar NR electron events observed by the LEFS60 telescope of the *ACE*/EPAM experiment. The algorithm can be easily adapted to study sectored time-intensity profiles measured by other telescopes on board spacecraft with similar features and performance.

4.1 Fitting procedure

4.1.1 Deconvolution of the sectored intensities

We have developed a new technique for deconvolving the effects of interplanetary transport in order to determine the underlying time profile of particle injection near the Sun. We solve the inversion problem of obtaining the mean free path and the injection time profile at the

Sun from a set of measured sectored intensities $I_l^s(t)$, where $I_l^s(t)$ is the intensity measured at time t by the sector s in the energy channel $[E_l, E_l + \Delta E_l]$. By taking into account the angular response of the EPAM/LEFS60 telescope (see Chapter 2), we derive the modeled sectored intensities $M_l^s(t; \lambda_r)$, in sector s and energy interval l, that have to be compared with $I_l^s(t)$.

We consider an arbitrary function $q(t)$ – to be determined – that represents the injection function of NR electrons close to the Sun. Then, M_l^s can be written as

$$M_l^s(t; \lambda_r) = \int_{T_1}^{T_2} dt' g_l^s(t, t'; \lambda_r)\, q(t'), \tag{4.1}$$

where $g_l^s(t, t'; \lambda_r)$ represents the contribution of an impulsive injection to the modeled intensities, for a given sector s and energy interval l, at a given time t, when the injection of NR electrons took place at time t', with $T_1 \leq t' \leq T_2$. Consequently, $M_l^s(t; \lambda_r)$ represents the modeled sectored intensities at time t, resulting from different elemental solar injections produced between T_1 and T_2. Details about the transformation of the simulated Green's function of particle propagation into $g_l^s(t, t'; \lambda_r)$ functions are given in Section 2.4.5. The calculation takes into account the angular response function of the EPAM/LEFS60 telescope and the angular directions scanned by the telescope as a function of time.

The injection energy spectrum is assumed to be a power-law, $dN/dE = CE^{-\gamma_s}$, terminated by cutoff energies $E_{\min}$ and $E_{\max}$. The energy spectrum is normalized to one particle per steradian at the solar surface. Therefore, $C = (\gamma_s - 1)/(E_{\min}^{1-\gamma_s} - E_{\max}^{1-\gamma_s})$. The spectral index, γ_s, is estimated from the observational data. Consequently γ_s is not a free parameter of the model.

The dependence of g_l^s (and thus of M_l^s) on ϵ has not been explicitly shown in Equation (4.1), because we regard ϵ as a descriptor of the scattering model rather than as a free parameter of the model (see section 3.3.2).

Taking discrete values of time, we have

$$M_l^s(t; \lambda_r) = \sum_{j=1}^{m} g_l^s(t_h, t'_j; \lambda_r)\, q(t'_j) \tag{4.2}$$

where $s = 1, 2, ..., 8$ numbers the sectors of the telescope. If n_{obs} is the number of observational time points in each sector, then $t_h = t_0 + (h - 1) \cdot \Delta t$, where Δt is the observational time resolution, t_0 is the origin of time of the event and $h = 1, 2, ..., n_{\text{obs}}$ numbers the observational time bins. Similarly $t'_j = T_1 + (j - 1) \cdot \Delta t$, where T_1 is the assumed origin of time of the injection of NR electrons ($T_1 < t_0$) and $j = 1, ..., m$ numbers the injection times. The duration of the injection ($T_2 - T_1$) determines the number of sectored Green's functions that need to

be computed. Therefore, in the energy range $[E_{\min}, E_{\max}]$, we choose T_2 to take the value

$$T_2 = (t_0 + n_{\rm obs} \cdot \Delta t) - \frac{z}{v_{\max}} \tag{4.3}$$

where z is the distance along the magnetic field line from the source to the observer and $z/v_{\max}$ corresponds to the transit time of the fastest particle considered in the analysis. We assume that injection starts after T_1, which is arbitrarily taken 30 min before the beginning of the observational type III burst radio burst[1] estimated at 14 MHz. Figure 4.1 illustrates the selection of the T_1 and T_2 injection parameters.

Equation (4.2) can be written as

$$M_l^s(t_h; \lambda_r) \equiv M_i(\lambda_r) = \sum_{j=1}^{m} g_{ij}(\lambda_r)\, q_j = (\mathbf{g} \cdot \vec{q})_i \tag{4.4}$$

where $i = h + (s-1) \cdot n_{\rm obs} = 1, 2, ..., n$ numbers the total number of observational points and $n = 8\, n_{\rm obs}$ gives the total number of observational points in all sectors; $\mathbf{g}$ is an $n \times m$ matrix with $(\mathbf{g})_{ij} = g_{ij}(\lambda_r)$.

Finally, the modeled intensities must be compared with the observations. Let b be the sector-averaged background intensity and $J_i = I_i - b$ with $I_i = I_l^s(t_h)$. We want to derive the m-vector $\vec{q}$ that minimizes the length of the n-vector $\vec{J} - \vec{M}$, that means solving the equation

$$\|\vec{J} - \vec{M}\| \equiv \|\vec{J} - \mathbf{g} \cdot \vec{q}\| \sim 0 \tag{4.5}$$

subject to the constraint that $q_j \geq 0\ \forall\, j = 1, 2, ..., m$. Thus, the best-fit $\vec{q} = (q_1, q_2, ..., q_m)$ corresponds to a comb of m delta-function injection amplitudes at times t_j. To obtain the best-fit values, we use the non-negative least squares (NNLS) method of Lawson & Hanson (1974), which always converges to a solution.

The total number of independent fitting parameters is m and the number of degrees of freedom is $n - m$, which is clearly much larger than the number of model parameters, as it should be. Note, however, that for a given interval of time, if the IMF vector has a polar angle equal to zero, all the sectors scan the same pitch-angle cosine range and therefore, we only get one independent sectored measurement instead of eight. This situation can be avoided by studying NR electron events observed by the LEFS60 telescope with μ-co $\geq 70\%$ (as explained in section 4.2.1).

[1] T_1 does not represent any constraint to the model neither introduces any bias in the results, provided that $T_1 \ll t_{\rm III}$. The value adopted is a compromise between such conditions and the computing time demanded if $(T_2 - T_1)$ is too large.

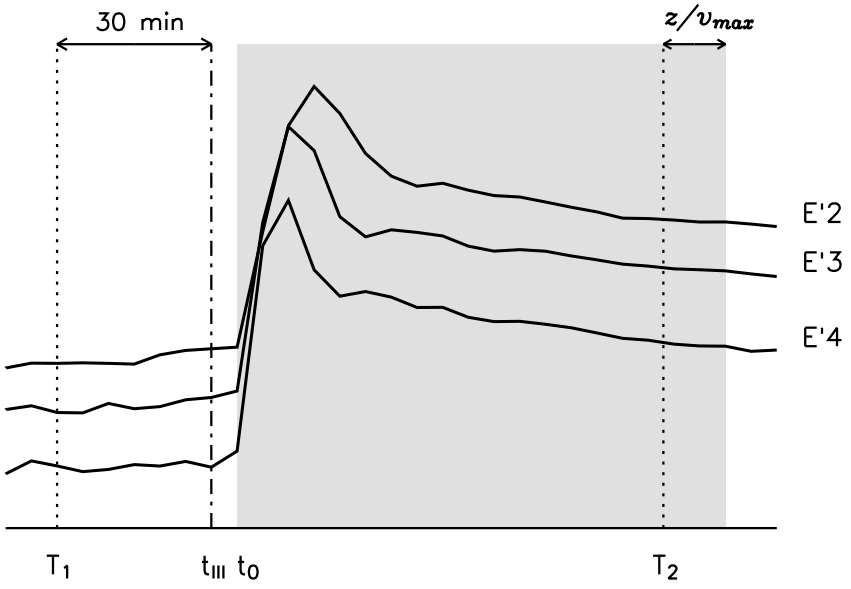

Figure 4.1: Illustration of the selection of the parameters T_1 and T_2. t_{III} marks the origin of the type III radio emission and t_0 indicates the origin of time of the event. The gray area shows the interval of time where the deconvolution technique is performed.

4.1.2 Injection function

The results of the transport simulation are given in terms of Green's functions normalized to one particle injected per steradian at the solar surface in the energy range $[E_{\min}, E_{\max}]$. From the deconvolution, we obtain $q(t) = \sum_{j=1}^{m} q_m \, \delta(t)$ i.e. a comb of m delta-function injection amplitudes in units of particles. We aim, however, to express the injection function by a histogram in units of particles per time unit and energy range. This can be obtained by dividing $q(t)$ by the observational time resolution, Δt, and by the energy range, ΔE, taken into account in the deconvolution.

If each energy channel is separately fitted, an extra factor has to be taken into account in order to normalize the results with respect to the channel. If the deconvolved energy channel ranges from E_1 to E_2, we have to take into account the fraction of the total simulated energy spectra covered by the channel; that is

$$A_c = \int_{E_1}^{E_2} C E^{-\gamma_s} \, dE, \tag{4.6}$$

where C is the normalization constant, $\int_{E_{\min}}^{E_{\max}} C E^{-\gamma_s} \, dE = 1$, given by $C = (1 - \gamma_s)/(E_{\max}^{-\gamma_s+1} - E_{\min}^{-\gamma_s+1})$. Therefore,

$$A_c = \frac{E_{\max}^{-\gamma_s+1} - E_{\min}^{-\gamma_s+1}}{E_2^{-\gamma_s+1} - E_1^{-\gamma_s+1}} \tag{4.7}$$

A_c represents the number of injected particles in the $[E_1, E_2]$ energy range, when we injected 1 particle in the $[E_{\min}, E_{\max}]$ energy range. Therefore, we need to divide the results by A_c in order to normalize the results with respect to the channel. Thus, the injection function histogram is given by

$$Q(t) = \frac{1}{A_c} \sum_{j=1}^{m} \frac{q_m}{\Delta t\, \Delta E} H(t - t_j)\, H(t_{j+1} - t) \tag{4.8}$$

4.1.3 Goodness of the fit

In addition to the injection function, the value of the mean free path that best fits the data has to be determined. The mean free path has a strong effect on the decay phase of the event. To take into account this influence (and the fact that the intensity may vary several orders of magnitude between the peak intensity and the later decay phase), we use the goodness-of-fit estimator

$$\zeta(\lambda_r) = \sum_{i=1}^{n} \left(\log \frac{I_i}{M_i^*(\lambda_r) + b} \right)^2 \tag{4.9}$$

to determine the best-fit value of λ_r. This estimator gives an equal weight to all relative residuals instead of just emphasizing the goodness of fit at the time of maximum. Here, $M_i^*(\lambda_r)$ is the best-fit model obtained from the NNLS algorithm for a given value of λ_r. Note that minimizing ζ implies minimizing logarithmic differences between the observational data and the modeled data.

4.2 Deconvolution test

In this section, we test the deconvolution technique outlined in the previous section. We aim to deconvolve synthetic sectored intensity profiles in order to verify that we recover the injection profile, the description of the scattering processes and the value of the radial mean free path originally assumed. Furthermore, we aim to set constraints on the conditions under which the application of the deconvolution algorithm is reliable. The deconvolution test is divided in two parts. First, we produce synthetic data in five main steps:

1. Simulation of the Green's function of particle transport for several values of the radial

mean free path, $0.1 \leq \lambda_r \leq 1.4$ AU, and different scattering models.

2. Selection of: (i) a scattering model and a value of λ_r ; and (ii) an injection profile.

3. Convolution of the Green's function of particle transport for the selected λ_r by the selected injection profile.

4. Selection of a magnetic field configuration and, therefore, of the μ-co of the telescope.

5. Calculation of the synthetic observational sectored intensities (from steps 3 and 4).

Second, we deconvolve the synthetic observational sectored intensities and check the goodness of the fit in each case. Finally, we verify that the best fit corresponds to the original λ_r and that the underlying injection profile is resolved.

We assume that the particle injection of NR electrons takes place at the root of a Parker spiral magnetic field ($u = 425$ km s^{-1}). The energy spectrum at the source is assumed to be $dN/dE \propto E^{-2.9}$ in the energy range 62–330 keV. The maximum simulation time is fixed to 120 min. The detector is assumed to have a time resolution of 72 s and to record in a single energy range 175–312 keV (it corresponds to E'4 of EPAM/LEFS60).

We consider three different scattering cases: isotropic and μ-dependent scattering with $\epsilon = 0.10$ and $\epsilon = 0.01$. For each scattering case we simulate sixteen values of the radial mean free path between 0.1 and 1.6 AU with step intervals of 0.1 AU – a total of 48 different scenarios.

We select two of these scenarios to test the deconvolution technique: $\lambda_r = 0.2$ AU and $\lambda_r = 0.9$ AU, for the μ-dependent scattering case with $\epsilon = 0.01$. As discussed in the introduction, several studies suggest that NR electron events are produced by an impulsive injection component related to the flare and a more time extended component associated with the CME-driven shock. We aim to determine whether the deconvolution technique is able to resolve two components of this kind. Therefore, we assume that the injection close to the Sun takes place in two episodes: a short intense injection lasting ~4 min and injecting 3×10^{33} electrons followed by a weaker decaying injection component starting 72 s later and injecting 3×10^{31} electrons to the interplanetary medium. Figure 4.2 illustrates the assumed injection profile.

We convolve the Green's functions of particle transport for $\lambda_r = 0.2$ AU and $\lambda_r = 0.9$ AU and a μ-dependent scattering model with $\epsilon = 0.01$ by the injection profile illustrated in Figure 4.2. Figure 4.3 shows the resulting 175–312 keV omni-directional intensities for $\lambda_r = 0.2$ AU (Event 1) and $\lambda_r = 0.9$ AU (Event 2), respectively. The inset plots show three snapshots of the pitch-angle distributions (normalized to maximum): during the rising phase, at the peak and

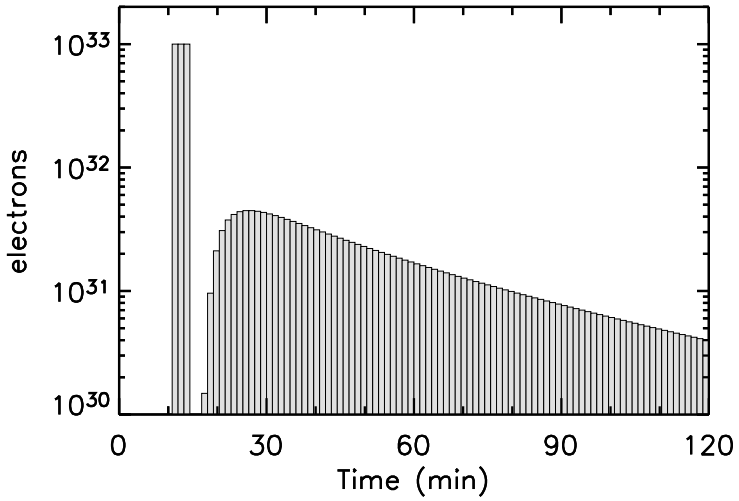

Figure 4.2: Two component solar injection profile.

during the decay phase of the event (indicated by black dots on the time-intensity profile). As can be seen, the shorter the mean free path

- the later first particles are detected at the spacecraft position,
- the later the particle omni-directional intensity profile peaks,
- the lower the intensity of the peak is,
- the slower the decay phase is,
- the higher the intensities are in the decay phase of the event,
- the more isotropic the pitch-angle distributions are late in the event.

Nevertheless, sectored intensity profiles observed by a detector mounted on a spinning spacecraft will be rather different from these two synthetic differential intensities because the IMF orientation does not always allow all particles moving across 1 AU to be recorded.

In the following subsections, we verify that the deconvolution technique outlined in the previous sections is correct. For this purpose, we neglect measurement errors of the detector and we study the different representations that these two events take depending on the magnetic field configuration. We study two cases: (1) a synthetic magnetic field vector that does not vary with time; (2) two selected magnetic field configurations obtained from observations by the *ACE*/MAG instrument. Once the magnetic field configuration is known, we can calculate the sectored intensities observed by the LEFS60 telescope for these two events (see Chapter 2). We also assume that the background intensity of the sectors is 10 e/(cm^2 sr s MeV). Then,

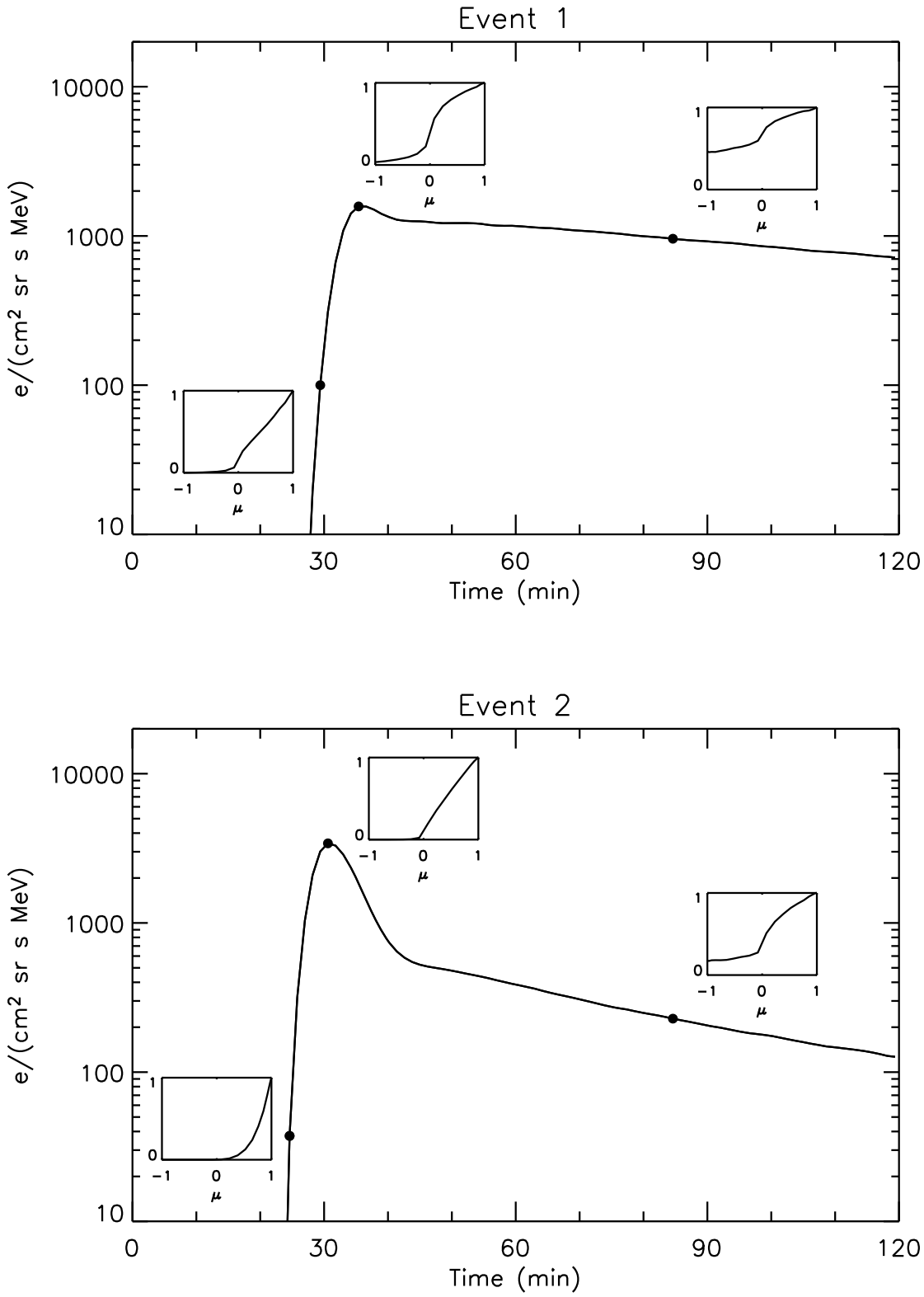

Figure 4.3: 175–312 keV omni-directional intensities for Event 1 ($\lambda_r = 0.2$ AU and μ-dependent scattering with $\epsilon = 0.01$), top panel, and for Event 2 ($\lambda_r = 0.9$ AU and μ-dependent scattering with $\epsilon = 0.01$), bottom panel. The three insets in each plot show the pitch-angle distributions (normalized to maximum) corresponding to the snapshots indicated by dots.

we can deconvolve the sectored events for the 48 situations detailed above. We select the time interval between $t_0 = 15$ min and 120 min to apply the deconvolution technique and we assume that the solar injection starts after $T_1 = 0$ min.

4.2.1 Stable synthetic magnetic field

Let us assume a magnetic field vector that does not vary with time. As a representative case, we choose $\hat{B}$ perpendicular to the spin axis, with polar angle $\theta_B = 90°$ and clock-angle $\phi_B = 60°$, in the spacecraft coordinate system. For this configuration, the telescope gets nearly complete coverage in pitch-angle cosine during the whole event; μ-co $\simeq 100\%$ (see section 2.4.4). Figure 4.4 displays the intensities observed by each sector (top) and the pitch-angle cosine, μ, of each sector (bottom) for the two events synthesized. Since the magnetic field vector does not vary with time, these values remain constant throughout the event.

Note that the sectors scanning particles with $\mu \simeq 1$ are the ones that start earlier to observe particles and that record higher intensities, whereas those sectors with $\mu < 0$ start to observe particles later in time and measure lower intensities with more gradual increases. The small fluctuations seen in the decay phase of the intensity profiles are statistical.

Figure 4.5 shows the values of the goodness of fit estimator, ζ, obtained from the deconvolution of the two events shown in Figure 4.4, for the 48 tested scenarios; the left panel shows Event 1 and the right panel shows Event 2. Each curve[2] displays the values of ζ for a different scattering case: isotropic (dashed line), μ-dependent with $\epsilon = 0.10$ (dotted line) and μ-dependent with $\epsilon = 0.01$ (solid line). Open circles indicate the lowest value of ζ, $\zeta_{\min} = \zeta(\lambda_{\min})$, obtained for each case.

As can be seen in Figure 4.5, $\zeta(\lambda_r)$ has a single minimum and is rather symmetric around $\lambda_{\min}$. The ζ-values are high for $\lambda_r < \lambda_{\min}$ because for these values of λ_r it is not possible to reproduce the rising phase of the event. No matter what the injection profile is, particles with smaller λ_r get to the observer too late to reproduce the detected onset (if injection is assumed to start after $T_1 = 0$ min). For Event 1, the ζ-values obtained for the three scattering cases at $\lambda_{\min}$ are very similar. This is because for a low value of λ_r, differences between normalized PADs are small (see Figure 3.4). The lowest value, $\zeta = 0$, is obtained for μ-dependent scattering with $\epsilon = 0.01$ and $\lambda_r = 0.2$ AU for Event 1, and $\lambda_r = 0.9$ AU for Event 2. In these two cases the injection profile obtained from the deconvolution reproduces the actual injection profile (see next paragraph). We therefore conclude that the deconvolution

[2] Actually, we compute the values of the goodness of fit estimator, ζ, for a grid of values of λ_r. It is possible to increase the number of values of λ_r to get a denser grid, but the results will not differ significantly from the general trend shown in Figure 4.5.

technique provides accurate results if the coverage of the telescope is of ∼100%.

Figure 4.6 illustrates the injection profile yielded by the deconvolution algorithm as a function of the radial mean free path derived for μ-dependent scattering with $\epsilon = 0.01$. For Event 1 and $\lambda_r < 0.2$ AU, the deconvolution algorithm yields an earlier and higher impulsive injection, and a high value of ζ. As expected, a minimum of $\zeta = 0$ is found for $\lambda_r = 0.2$ AU; in this case, the derived injection profile matches the original assumption. As λ_r increases, the deconvolved injection profile becomes wider but ζ increases again because the prolonged injection produces high anisotropies that cannot adequately fit the intensities registered by the sectors not aligned with the magnetic field. The same type of explanation is valid for Event 2, but $\zeta_{\min} = 0$ occurs for $\lambda_r = 0.9$ AU as expected.

To get an idea of the sensitivity of the deconvolution algorithm, we study the results yielded by the algorithm if we were assuming a scattering model that badly describes the scattering processes at work. In the cases we are studying, Event 1 and Event 2, this would correspond to fit these events assuming either isotropic scattering or μ-dependent scattering with $\epsilon = 0.10$. For Event 1, the best fit corresponds to $\lambda_r = 0.2$ AU for these two scattering cases; the injection profiles are shown in the two bottom left panels of Figure 4.7. In these two cases, two injection episodes can be resolved but, (i) the onset of the first prompt injection is blurred by erroneous previous weaker injection episodes and (ii) the onset of the second injection is delayed and its decay phase shows noticeable intermittency. For Event 2, the best fit corresponds to $\lambda_r = 0.8$ AU for the two scattering cases. Thus, if we were to erroneously assume an isotropic or a μ-dependent scattering model with $\epsilon = 0.10$, we would underestimate the value of λ_r. For isotropic scattering and $\lambda_r = 0.8$ AU, the obtained injection profile displays a single injection episode, but is one that is modulated by the two actual episodes (Figure 4.7, bottom right panel). For μ-dependent scattering with $\epsilon = 0.10$ and $\lambda_r = 0.8$ AU, the two injection episodes can be resolved but they start earlier than the actual injection profile does (Figure 4.7, middle right panel). Thus, the more accurate the description of the scattering processes at work, the better the injection profile can be resolved.

An important issue to address is how the pitch-angle cosine coverage of the telescope, μ-co, influences the results of the deconvolution. For this purpose, we study eight different magnetic field configurations that assure four different values of the μ-co of the LEFS60 telescope (85%, 70%, 55% and 40%). Table 4.1 lists the characteristics of these eight magnetic field configurations; the first column identifies the configuration, the second column gives the μ-co; then follows the corresponding $\mu_{\max}$ and $\mu_{\min}$ scanned by the telescope[3]; the last two columns give the polar angle and the clock-angle of the magnetic field vector in the space-

[3]If $\mu_{\max}$ is negative, the telescope only observes the negative hemisphere of the PAD, whereas if $\mu_{\min}$ is positive, the telescope is only able to observe the positive hemisphere.

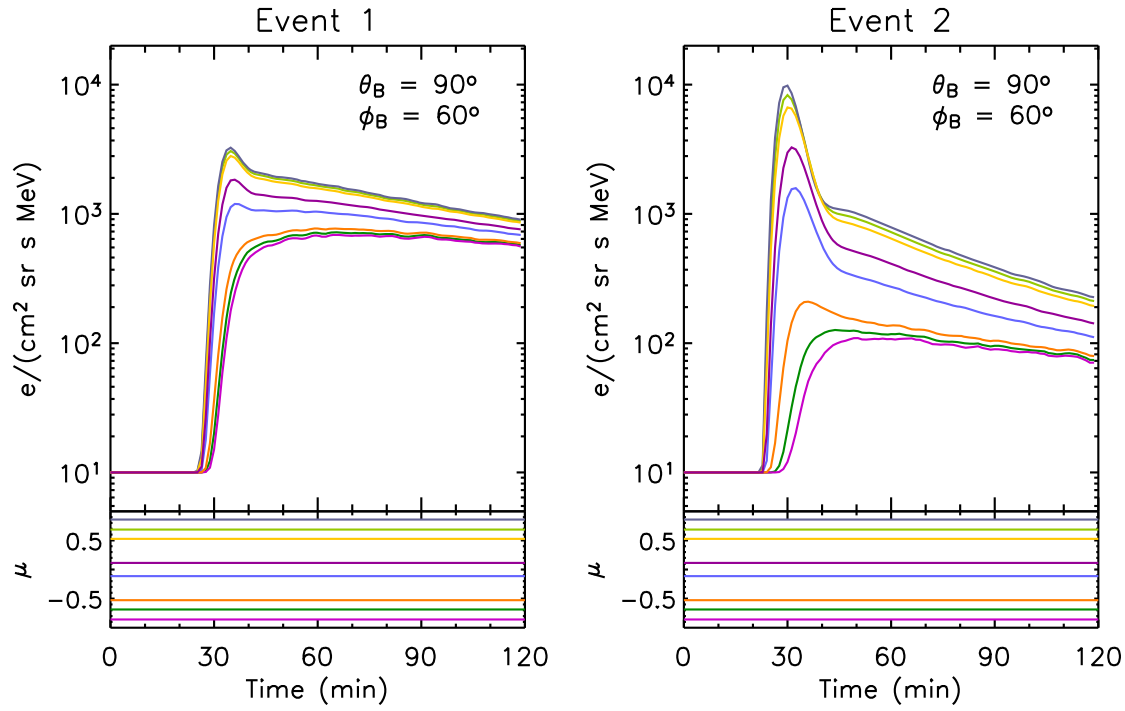

Figure 4.4: Event 1 and Event 2 as observed by the LEFS60 telescope for a constant magnetic field vector. Different colors represent different sectors. Upper panels show the electron sectored intensities 175–312 keV. Lower panels show the pitch-angle cosine scanned by each sector.

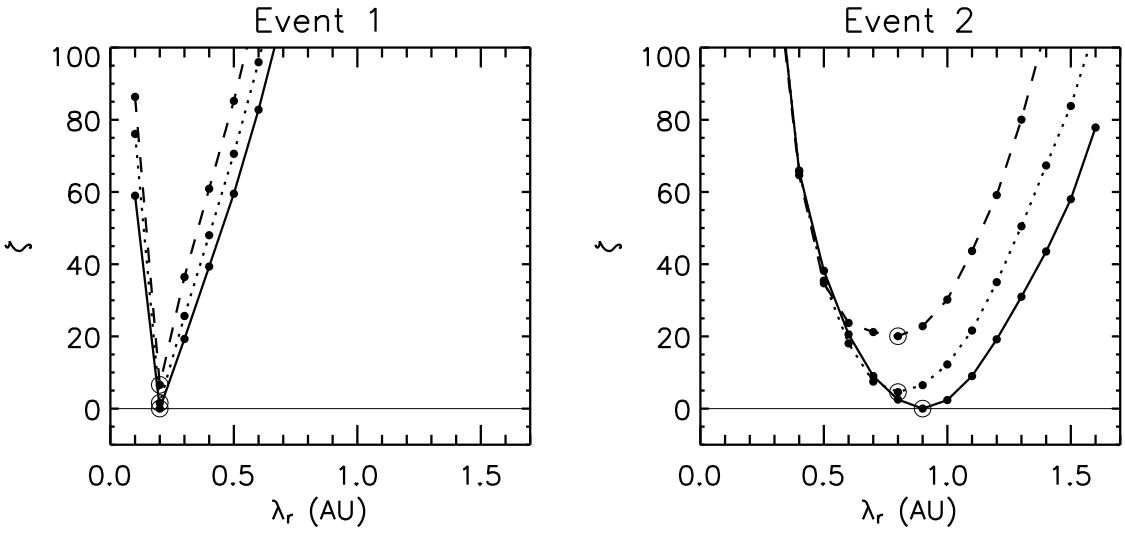

Figure 4.5: Goodness of fit estimator, ζ, obtained from the deconvolution of Event 1 and 2 for 16 values of the radial mean free path and three scattering models: isotropic (dashed line), μ-dependent scattering with $\epsilon = 0.10$ (dotted line) and with $\epsilon = 0.01$ (solid line). The magnetic field vector is assumed to have $\theta_B = 90°$ (μ-co $\simeq 100\%$) and $\phi_B = 60°$. The lowest ζ value, ζ_{min}, is marked by an open circle. The thin horizontal line shows $\zeta = 0$.

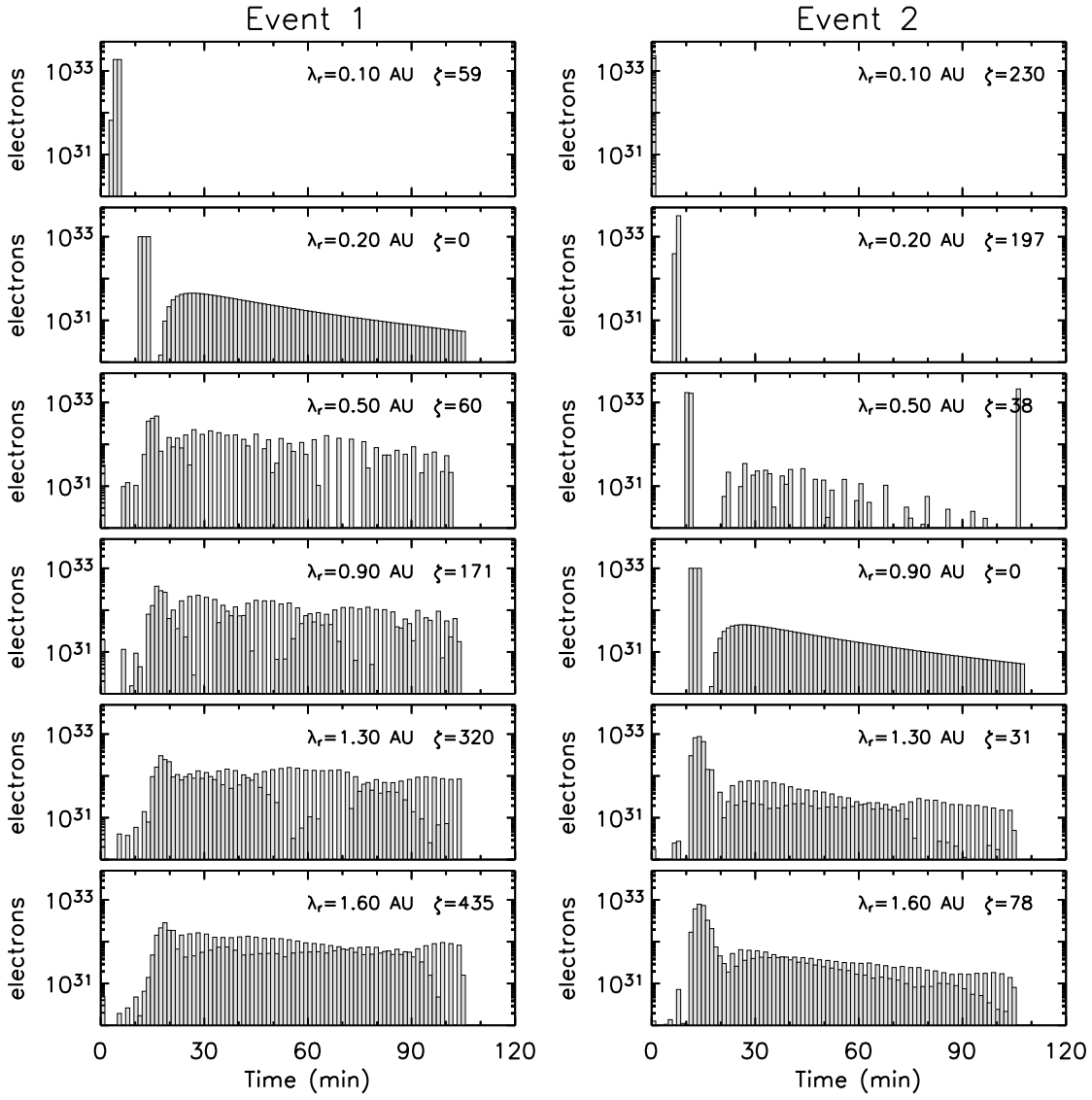

Figure 4.6: Electron injection profiles as a function of λ_r for μ-dependent scattering with $\epsilon = 0.01$. Left panel displays the results for Event 1, right panel for Event 2.

craft coordinate system. Each configuration is labeled with a number. Configurations with the same number have the same μ-co and the prima denotes that the telescope mostly observes negative pitch-angle cosines. Figure 4.8 illustrates the μ-co of the eight magnetic field configurations (left) and the range of μ scanned by the telescope in each case (right).

As an example, Figure 4.9 displays the intensities observed by each sector and the pitch-angle cosine of the zenith direction of the detector at the midpoint clock angle of the sector, as a function of time, for Event 1 and Event 2 and for the configurations (2') and (4), and (2) and (4'), respectively. Note that the narrower the range of μ scanned by the telescope, the more similar the intensity profiles registered by different sectors. Moreover, the smaller $\mu_{\max}$, the lower the intensities registered by the telescope.

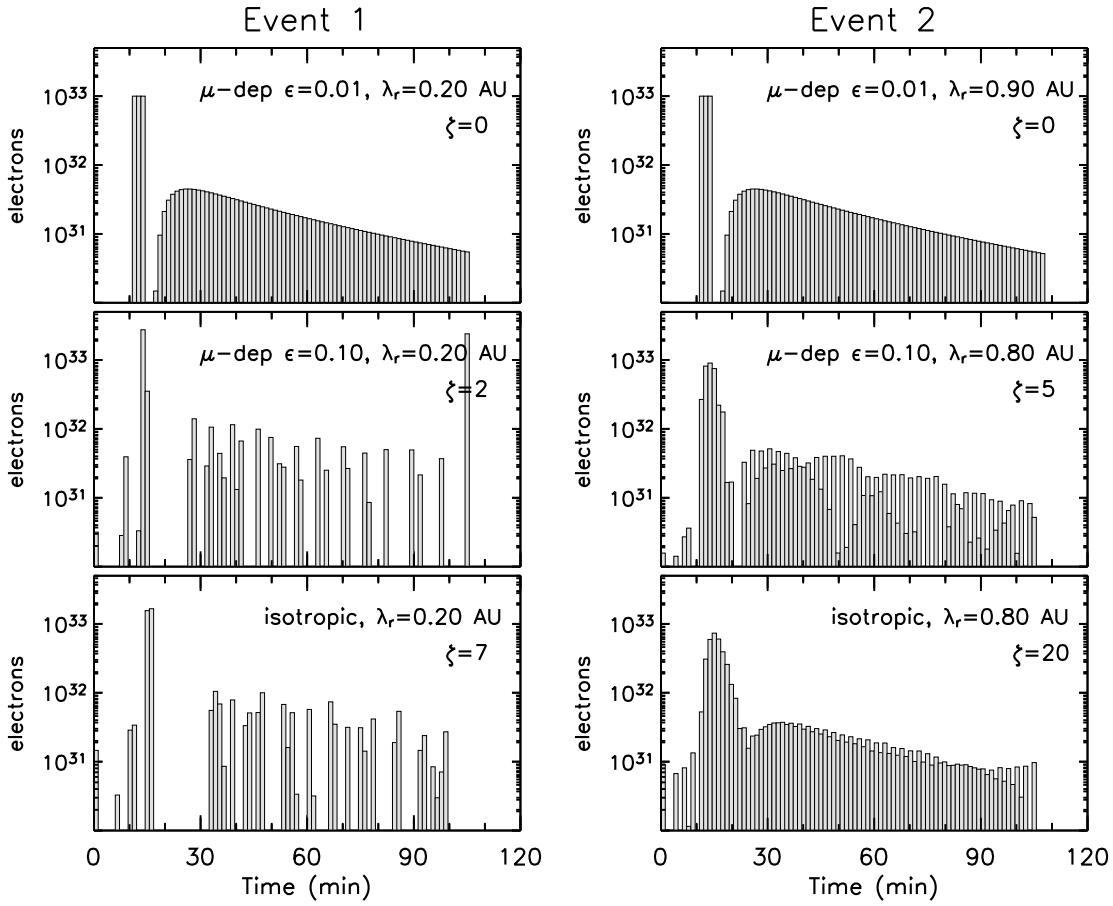

Figure 4.7: Best-fit electron injection profiles as a function of the scattering model for Event 1 (left) and Event 2 (right), assuming $\theta_B = 90°$ (μ-co $\simeq 100\%$) and $\phi_B = 60°$.

Figure 4.10 shows the values of the ζ-estimator obtained from the deconvolution of Event 1. Each one of the eight panels corresponds to a different magnetic field configuration (and thus, Event 1 is observed differently by the LEFS60 telescope). Panels in the same row show the results for the same value of μ-co. Panels in the same column show values of μ-co that decrease from top to bottom.

From this figure, it is clear that the higher the μ-co of the telescope the deeper the minimum of ζ and the more symmetric the function $\zeta(\lambda_r)$ around the best fit value of λ_r. If $\lambda_r < 0.2$ AU, ζ values remain high for any magnetic field configuration due to the onset effect. On the other hand, if $\lambda_r > 0.2$ AU the lower the μ-co, the flatter the $\zeta(\lambda_r)$. If $\zeta(\lambda_r)$ becomes flat (i.e. the ζ-estimator takes similar values for a range of λ_r), it means that there is more than one scenario that reasonably fit the observational data. Thus, the information contained in the measurements is not enough to discern the actual scattering model, the value of λ_r or the underlying injection profile. This is what happens when μ-co $= 40\%$ (configurations 4), where all sectors scan nearly the same range of μ values.

Table 4.1: Characteristics of the magnetic field configurations.

	LEFS60 coverage			$\hat{B}$	
	μ-co	$\mu_{\min}$	$\mu_{\max}$	θ_B	ϕ_B
(1)	85%	-0.70	1.00	131.0°	60°
(1')	85%	-1.00	0.70	49.0°	60°
(2)	70%	-0.41	0.99	151.5°	60°
(2')	70%	-0.99	0.41	28.6°	60°
(3)	55%	-0.17	0.93	165.8°	60°
(3')	55%	-0.93	0.17	14.2°	60°
(4)	40%	0.04	0.84	177.6°	60°
(4')	40%	-0.84	-0.04	2.4°	60°

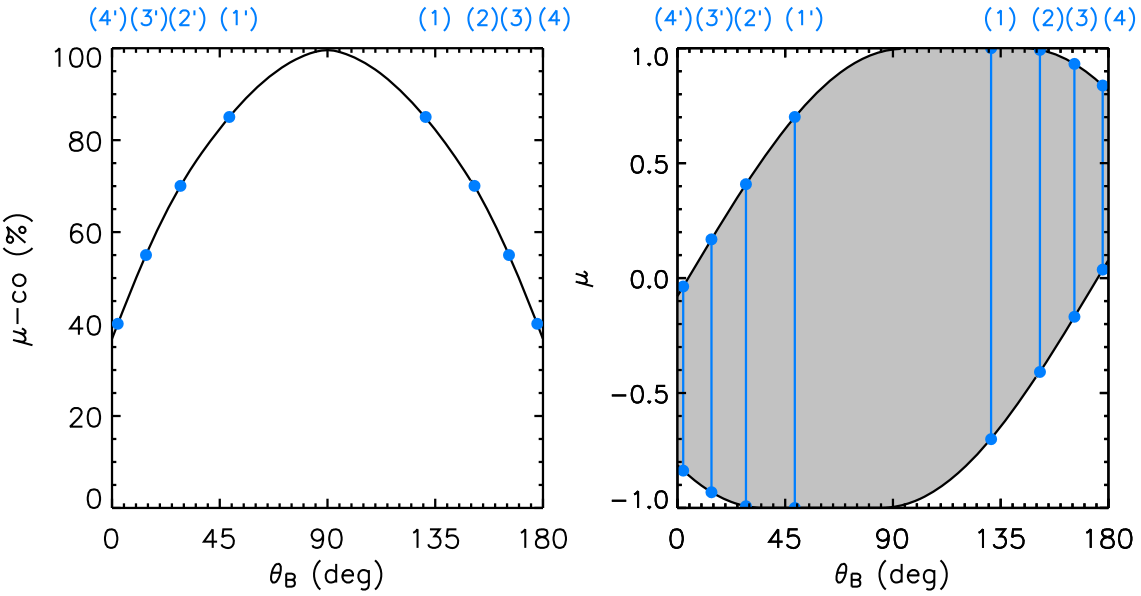

Figure 4.8: Left: μ-co of the LEFS60 telescope as a function of θ_B. Blue dots indicate the selected magnetic field configurations with μ-co equal to 85%, 70%, 55% and 40%. Right: Range of μ-values scanned for each configuration. Blue dots indicate the lowest and the highest values in each case; vertical blue lines mark the interval of coverage. The characteristics of the configurations are listed in Table 4.1.

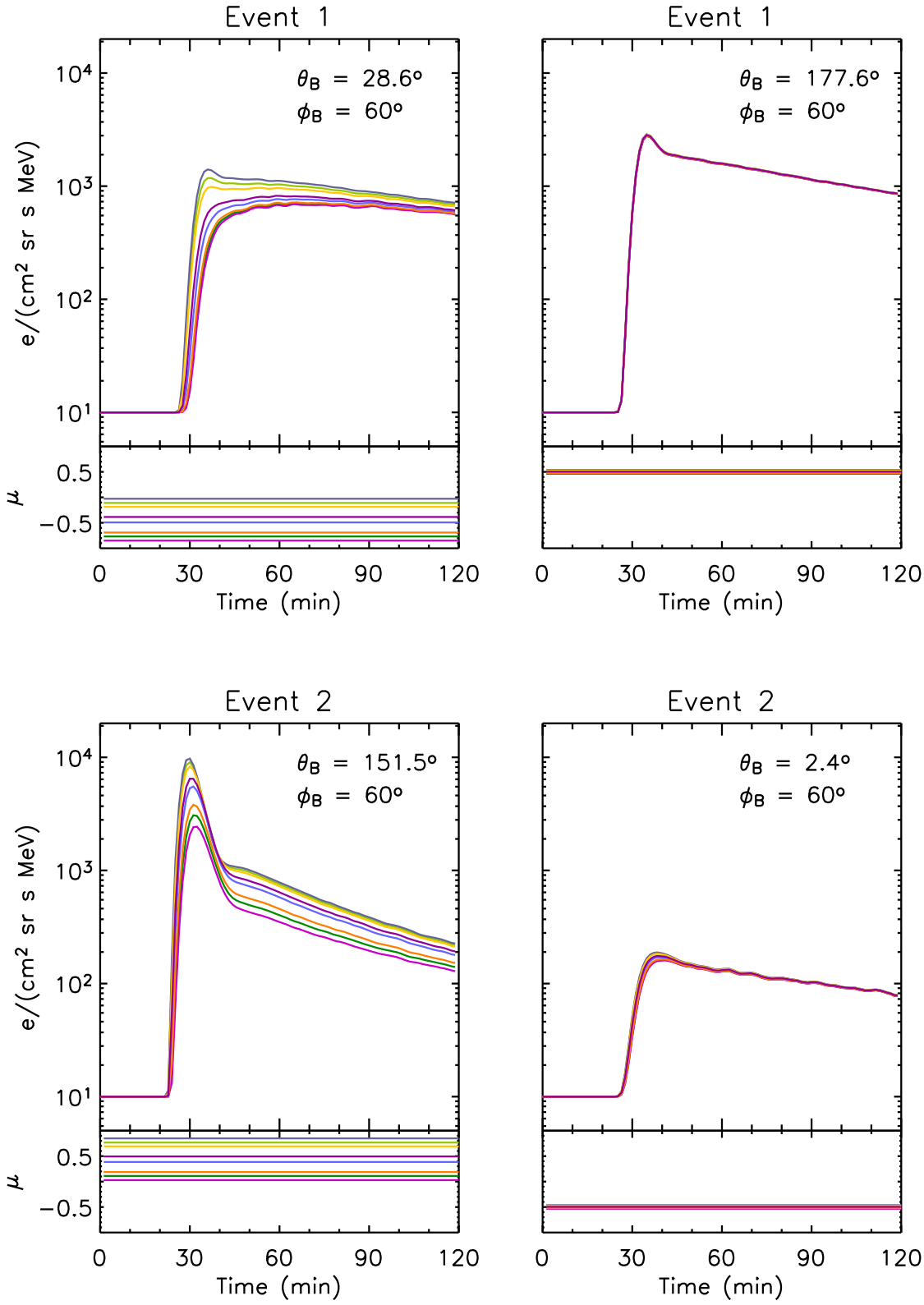

Figure 4.9: Event 1 and Event 2 as observed by the LEFS60 telescope for different magnetic field configurations. Same presentation as in Figure 4.4.

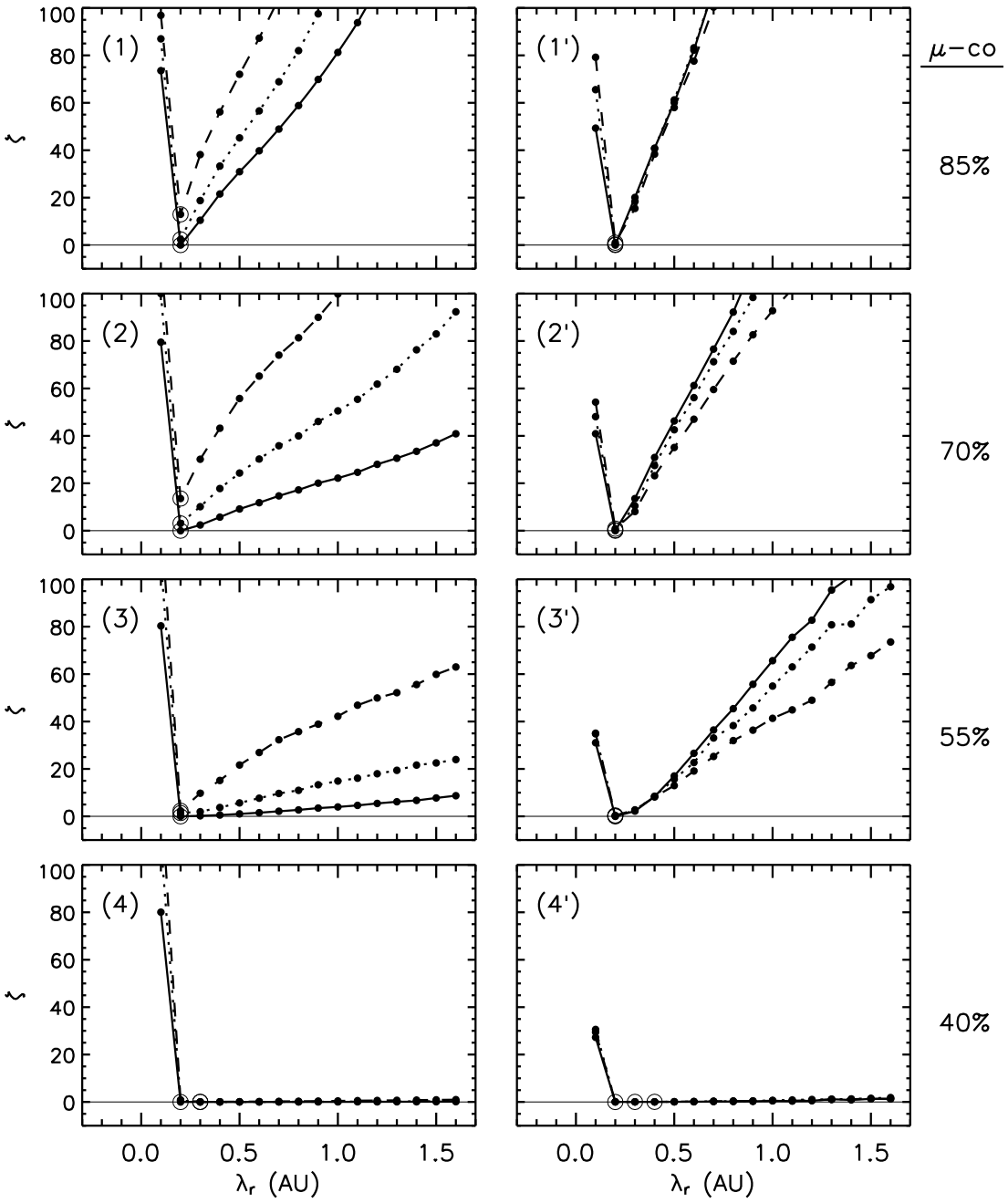

Figure 4.10: Goodness of fit estimator obtained from the deconvolution of Event 1 for 16 values of λ_r and three scattering cases: isotropic (dashed line), μ-dependent scattering with $\epsilon = 0.10$ (dotted line) and with $\epsilon = 0.01$ (solid line). Each panel shows the result for a different magnetic field configuration (details in Table 4.1). The lowest ζ obtained for each scattering case is denoted by an open circle. The thin horizontal line marks $\zeta = 0$.

Nevertheless, for all magnetic field configurations, the deconvolution technique obtains $\zeta = 0$ for μ-dependent scattering with $\epsilon = 0.01$, $\lambda_r = 0.2$ AU and an injection profile that coincides with the actual one; which shows that the technique works properly although it is no longer possible to distinguish the correct profile from the several possibilities.

By assuming isotropic scattering or a μ-dependent scattering with $\epsilon = 0.10$, we find that the best fit corresponds to $\lambda_r = 0.2$ AU in both cases, for configurations from 1 to 3 (Figure 4.10). For configurations (1) and (2), $\zeta_{\rm min}$ are different and the lowest one corresponds to μ-dependent scattering with $\epsilon = 0.01$. Note, however, that the $\zeta_{\rm min}$ values obtained for configuration (3) are very similar for the three scattering cases; therefore, for this configuration, it is not possible to distinguish between the three scattering models. This is a consequence of the lack of coverage of the telescope, in particular of $\mu \simeq 1$. These pitch-angle cosines are critical because they constrain the contribution of the injection. If $\lambda_r > 0.2$ AU, however, the evolution of $\zeta(\lambda_r)$ shows a different behavior for the three scattering models in configurations from (1) to (3). The more accurate the description of the scattering processes at work, the lower the value of ζ .

For configurations from (1') to (3'), deconvolution yields the same result, $\zeta \simeq 0$, for $\lambda_r = 0.2$ AU, for the three scattering cases. Therefore, it is not possible to discern the actual scattering processes at work, even when μ-co = 85%. This is because these configurations do not allow the telescope to scan particles with $\mu \sim 1$; the reverse of what happens in configurations (1) and (2). In addition, for $\lambda_r > 0.2$ AU, the evolution of $\zeta(\lambda_r)$ shows that the more isotropic the scattering model, the lower the value of ζ obtained.

Figure 4.11 shows the values of ζ obtained for Event 2 (using the same presentation as for Figure 4.10). As expected, the higher the μ-co of the telescope the deeper the minimum of ζ and the more symmetric the function $\zeta(\lambda_r)$ around $\lambda_{\rm min}$. For values of $\lambda_r > \lambda_{\rm min}$, the lower the μ-co, the flatter the $\zeta(\lambda_r)$. This is clearly seen when μ-co $\leq 55\%$. For all magnetic field configurations, the deconvolution algorithm gives $\zeta = 0$ for μ-dependent scattering with $\epsilon = 0.01$, $\lambda_r = 0.9$ AU and an accurate injection profile.

By assuming either isotropic scattering or μ-dependent scattering with $\epsilon = 0.10$, we find that the obtained $\lambda_{\rm min}$ value underestimates the actual value of λ_r for configurations from (1) to (3), whereas it is overestimated for configurations from (1') to (3'). Also, as expected, for configurations (1) and (2), $\zeta_{\rm min}$ is different for the three scattering cases, while for configurations (1') and (2') the values of $\zeta_{\rm min}$ are very similar in the three cases. The evolution of $\zeta(\lambda_r)$ for $\lambda_r > 0.9$ AU for the three scattering models in configurations 1 to 3 follows the same explanation given for Figure 4.10.

Thus, we conclude that in order to discern the actual scattering model, the value of λ_r and the underlying injection profile from LEFS60 sectored measurements of NR electron

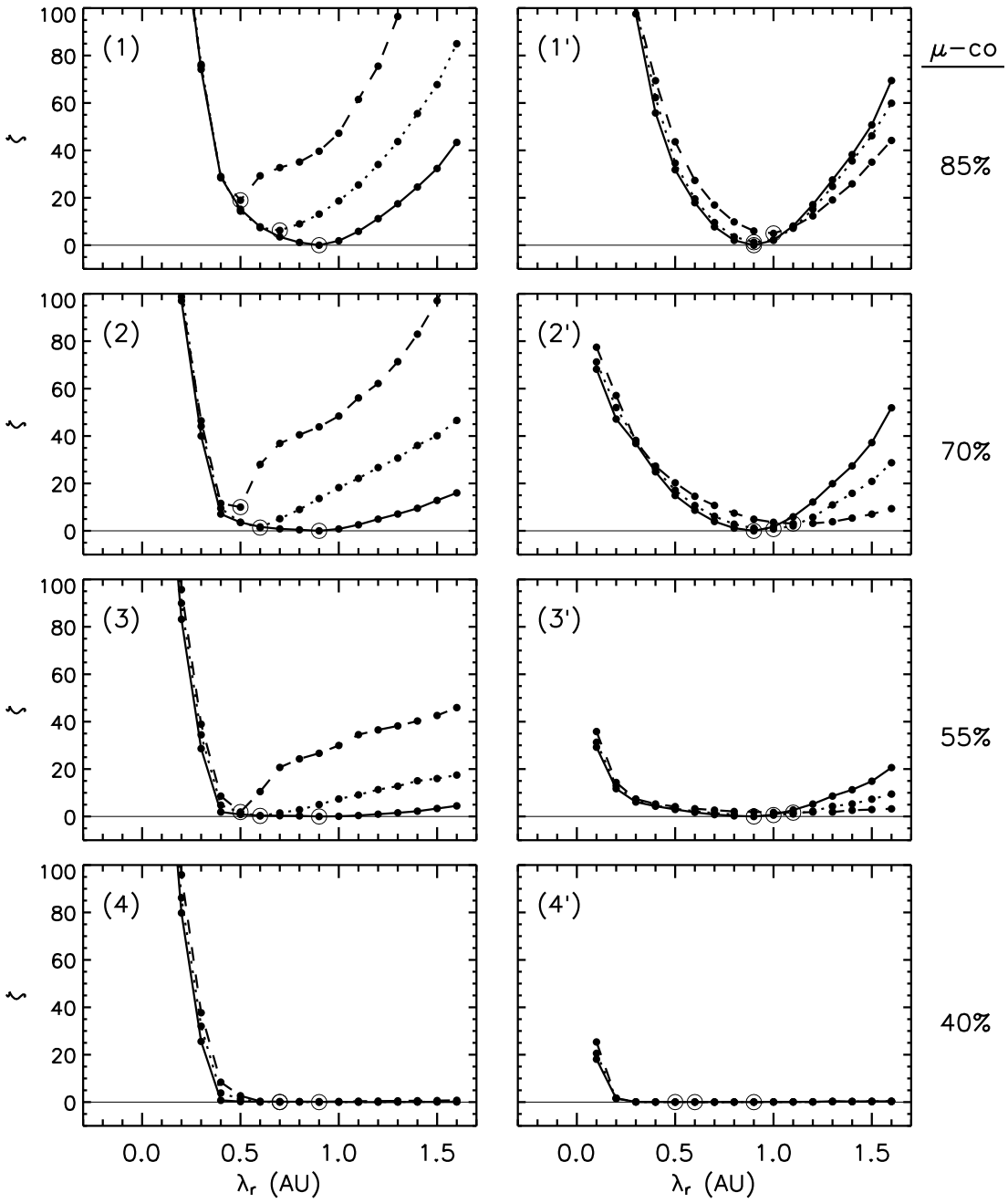

Figure 4.11: Goodness of fit estimator obtained from the deconvolution of Event 2. Same presentation as in Figure 4.10.

intensities two requirements must be fulfilled:

1. the event must be observed with μ-co $\geq 70\%$, and
2. the telescope must scan particles coming antisunward along the field direction.

4.2.2 Varying magnetic field

We select two different time periods during which the *ACE*/MAG instrument measured the local magnetic field vector in the spacecraft coordinate system with low and high variation of θ_B and ϕ_B, respectively. We label these two data sets as configurations (5) and (6). They correspond to the time periods from 17:45 UT to 19:45 UT on 2004 September 19 (5), and from 14:00 UT to 16:00 UT on 2001 April 15 (6). The magnetic field vector shows a standard deviation in θ_B of 14° and 31°, respectively, and a standard deviation in ϕ_B of 9° and 42°. The mean μ-co of the telescope during these periods is very similar μ-co $\simeq 90\%$. Table 4.2 lists the characteristics of these two data sets. The first column identifies the magnetic field configuration; the following three columns give the date and the time period of the MAG measurements; the next three columns give the mean polar angle and the mean clock-angle of $\vec{B}$ in the spacecraft coordinate system and its prevailing polarity; the last column gives the mean μ-co of the telescope during the selected time period.

The sign of the magnetic field (polarity) is relevant to the calculation of the pitch-angle distributions. A negative IMF polarity means that the field-aligned electrons coming from the Sun have a pitch-angle cosine $\mu = -1$, whereas a positive IMF polarity means that anti-sunward field-aligned electrons have $\mu = +1$. A change of polarity during the period of study of the event may indicate a change in the flux tube scanned by the spacecraft, implying a possible change in the injection history and interplanetary transport conditions of the energetic particles.

In the Radial Tangential Normal (RTN; spacecraft centered) coordinate system[4], R is the outward Sun to spacecraft radial component, T is the component perpendicular to R in the ecliptic plane in the sense of solar rotation, and N completes the orthogonal set pointing toward the North. We define the polarity of the interplanetary magnetic field as

$$\text{sign}(\vec{B}) = \text{sign}(B_R - B_T) \tag{4.10}$$

where B_R and B_T are the R and T components of the magnetic field vector in the RTN coordinate system, respectively. Figure 4.12 illustrates how the polarity changes as a function of

[4] http://www.srl.caltech.edu/ACE/ASC/coordinate_systems.html

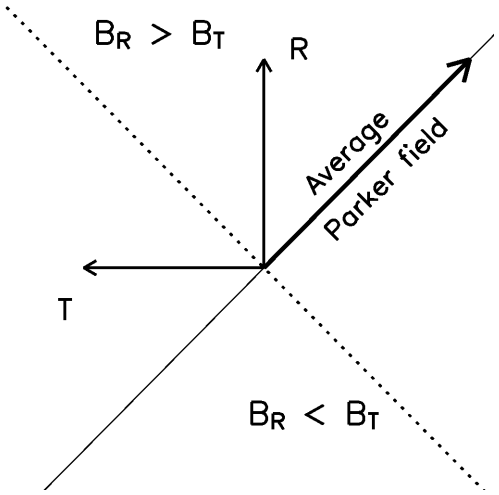

Figure 4.12: Average Parker field direction at 1 AU. R shows the outward Sun to spacecraft radial direction and T is the component perpendicular to R in the ecliptic plane in the sense of solar rotation. Dotted line separates regions where $B_R > B_T$ (positive polarity) and $B_R < B_T$ (negative polarity).

the interplanetary magnetic field direction.

From the MAG measurements of B_R and B_T at 1 AU at 72 s time resolution for the time periods listed in Table 4.2, we calculate the polarity of the interplanetary magnetic field as a function of time and estimate the modal value (+1 or -1) during the period of study of the event.

Figure 4.13 shows the magnetic field measurements and the range of μ-values scanned by the LEFS60 telescope, for the two configurations; (5) left and (6) right. The top panel shows the IMF magnitude and its polarity (thin line). The two middle panels show θ_B and ϕ_B in the spacecraft coordinate system. The bottom panel shows the range of μ-values scanned by the LEFS60 telescope (gray area) and the pitch-angle cosine of each sector as a function of time.

The IMF polarity is positive and constant for configuration (5). For configuration (6), however, the polarity is negative during most of the period under study (this means that electrons coming from the Sun along the field lines have $\mu = -1$) but there are some reversals after 19:05 UT. For the deconvolution procedure and for the estimation of the goodness of the fit, we only consider those data points showing the modal polarity.

Figure 4.14 shows the ζ-values obtained from the deconvolution of Event 1 and Event 2 for configuration (5) and (6). The results for both configurations are quite similar to those obtained for configuration (1), with μ-co = 85 % and a stable magnetic field (section 4.2.1). Therefore, we conclude that the variation of the magnetic field direction does not change the results of the deconvolution, provided that final requirements listed for a stable magnetic field are met and that changes in polarity are taken into account.

Table 4.2: Magnetic field data sets selected from EPAM/MAG instrument.

	Time period			$\vec{B}$			
	Date			$<\theta_B>$	$<\phi_B>$	polarity	μ-co
(5)	2004 Sep 19	17:45	19:45	$120° \pm 14°$	$3° \pm 9°$	+1	90%
(6)	2001 Apr 15	14:00	16:00	$83° \pm 31°$	$-15° \pm 42°$	-1	91%

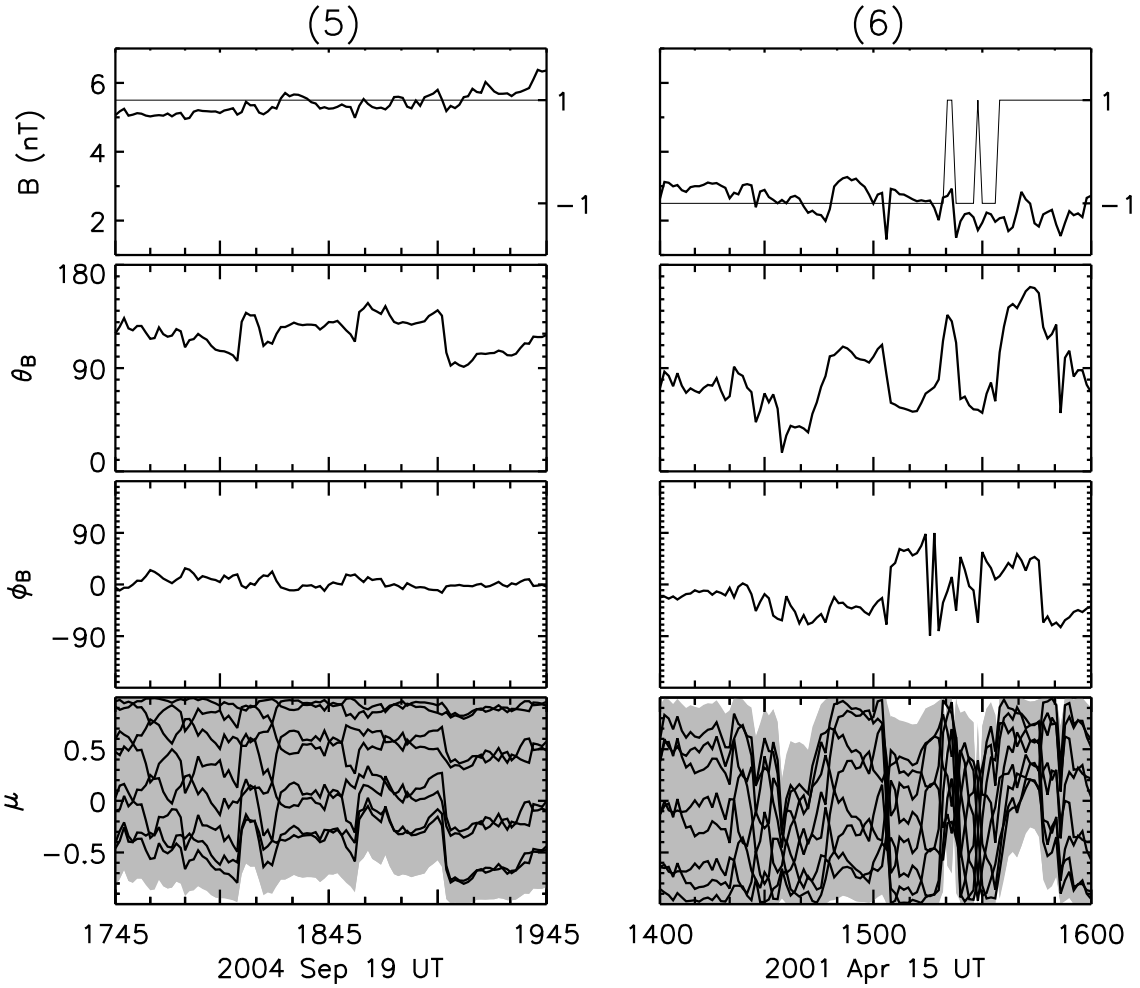

Figure 4.13: Three top panels: Magnetic field magnitude and polarity (thin line), polar angle (θ_B) and clock-angle (ϕ_B) measured by the MAG experiment in the spacecraft coordinate system during 2004 September 19 (left) and 2001 April 15 (right). Bottom panel: range of pitch-angle cosine scanned by the LEFS60 telescope (gray area) and the pitch-angle cosine of each sector as a function of time.

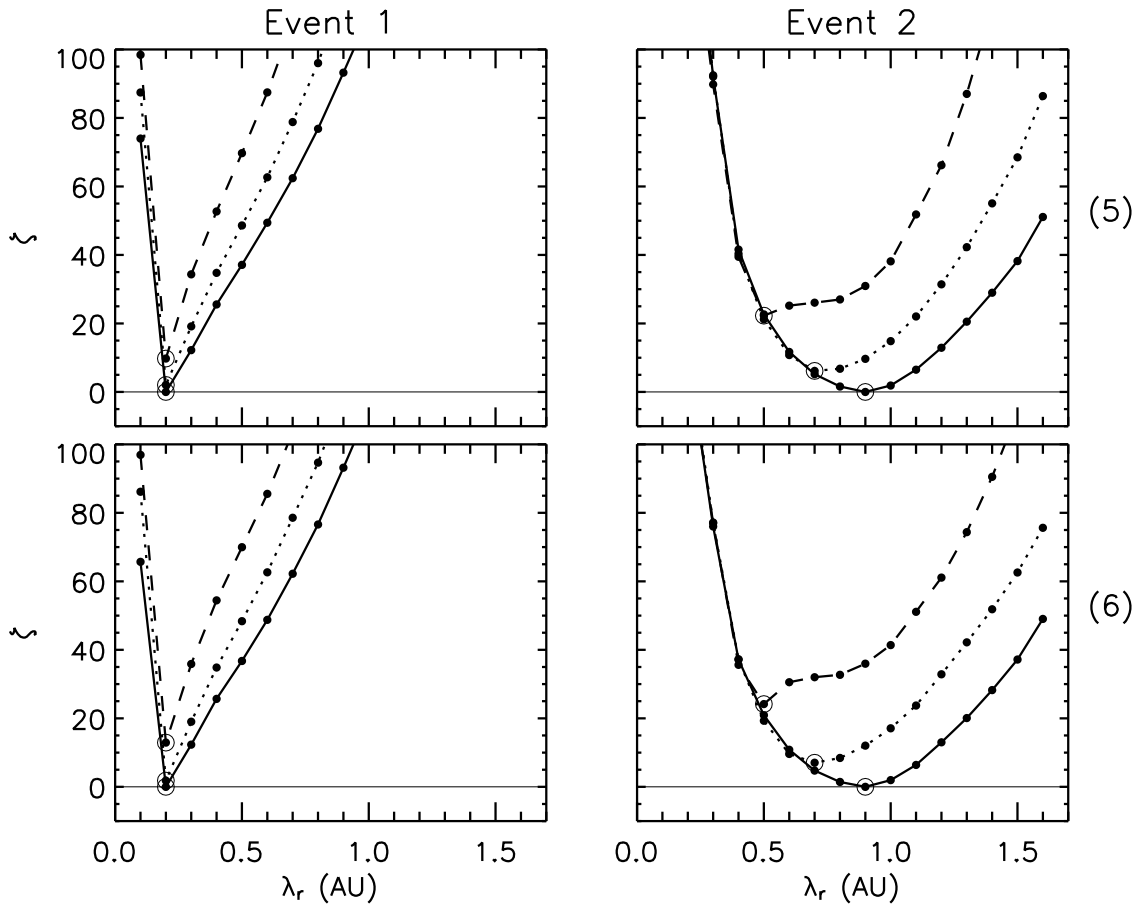

Figure 4.14: Goodness of fit estimator for magnetic field configurations (5), top, and (6), bottom, for Event 1 (left) and Event 2 (right). Same presentation as in Figure 4.5.

4.3 Measurement errors

In the previous section we assumed that intensity and magnetic field measurements have no errors associated. Real data, however, is generally subject to measurement errors. Thus, in the following two subsections we study how uncertainties, in either intensities or magnetic field directions, affect the results obtained by the deconvolution algorithm.

4.3.1 Intensity errors

Uncertainties in intensity data measured by EPAM are derived from statistical (counting) errors only, according to the EPAM Data Documentation[5]. Particle counting is a Poisson process. Therefore, the statistical error in counts is given by $\sqrt{N_s}$, where N_s is the number of counts registered in sector s in the averaging time period; thus, the relative error is given by $1/\sqrt{N_s}$. The sectored intensity, I_s, can be calculated by

$$I_s = \frac{N_s}{g \cdot \Delta t \cdot \Delta E} \tag{4.11}$$

where g is the geometrical factor in units of $\mathrm{cm}^2\mathrm{sr}$, Δt is the actual collection time in seconds, (that is, the livetime of each sector) and ΔE is the energy range in MeV. For the particular case under study, $g = 0.397$ cm^2 sr, $\Delta t = 9$ s and $\Delta E = 0.137$ MeV. Thus, the uncertainty, σ_s, associated with a measure of sectored intensity is given by

$$\sigma_s = \frac{I_s}{\sqrt{N_s}} \tag{4.12}$$

The effect of statistical errors in the results of the deconvolution algorithm can be studied by adding to the synthetic measured sectored intensities a random fraction of its associated error, that is, $I_s + \xi\sigma_s$, where ξ is a normally distributed random number (with zero mean and unit variance). We choose magnetic field configuration (5) and generate the sectored intensities observed by LEFS60 for Event 1 and Event 2. Afterward, we 'shake' the intensity data by adding $\xi\sigma_s$ to each data point. Finally, we try to fit the measured sectored intensities by means of the deconvolution algorithm.

Figure 4.15 shows the values of the goodness of fit estimator, ζ, obtained from the deconvolution of Event 1 and Event 2 when including statistical errors in the measured sectored intensities.

The values of $\zeta(\lambda_r)$ obtained for both events are quite similar to those obtained in section

[5] http://www.srl.caltech.edu/ACE/ASC/level2/epam_l2desc.html

4.2.2 for configuration (5) (see Figure 4.14), without taking into account the uncertainties in the intensity measurements.

The lowest ζ value, $\zeta = 0$, is obtained for μ-dependent scattering with $\epsilon = 0.01$ and $\lambda_r = 0.2$ AU for Event 1, and $\lambda_r = 0.9$ AU for Event 2. In these two cases, the injection profile obtained from the deconvolution reproduces the timing of actual injection profile but it shows intermittency in the time-extended injection component (see upper panels in Figure 4.16). We therefore conclude that the deconvolution algorithm tries to cope with fluctuating intensities by temporally switching on and off the injection.

To get an idea of the sensitivity of the deconvolution algorithm, we study the results yielded by the algorithm if we were assuming a scattering model that badly describes the scattering processes at work. In the cases we are studying, Event 1 and Event 2, this would correspond to fit these events assuming isotropic scattering or μ-dependent scattering with $\epsilon = 0.10$. For Event 1, the best fit corresponds to $\lambda_r = 0.2$ AU for these two scattering cases; the injection profiles are shown in the two lower left panels of Figure 4.16. In these two cases, two injection episodes can be resolved but, (i) the onset of the first prompt injection is blurred by previous weaker injection episodes, (ii) the onset of the second injection episode is delayed, and (iii) its decay phase shows noticeable intermittency. For Event 2, the best fit corresponds to $\lambda_r = 0.5$ AU for isotropic scattering and $\lambda_r = 0.7$ AU for μ-dependent scattering with $\epsilon = 0.10$. Thus, if we did not know that the actual scattering processes are described by a μ-dependent scattering with $\epsilon = 0.01$, in this case, we would underestimate the value of λ_r. In these two cases, the two injection episodes can be resolved (see two lower right panels of Figure 4.16) but they show the same characteristics as discussed for Event 1 (points from (i) to (iii)).

4.3.2 Magnetic field errors

Systematic errors are more probable in magnetic field data than in intensity measurements if we only compare sectored rates from one telescope. Therefore, we can test the effect of errors in the measurement of magnetic field directions by adding an offset of 0.05 nT, for example, to one of the magnetic field components. We choose magnetic field configuration (5) for this analysis, which is characterized by $\langle B_x \rangle = -4.5 \pm 0.7$ nT, $\langle B_y \rangle = -0.3 \pm 0.7$ nT and $\langle B_z \rangle = -2.6 \pm 1.1$ nT, and study the effects of an offset in the z component of the magnetic field.

We generate the sectored intensities observed by LEFS60 for Event 1 and Event 2. We then modify the magnetic field measurements by adding 0.05 nT to B_z. Finally, we try to fit the generated measured sectored intensities by calculating the Green's sectored intensities using

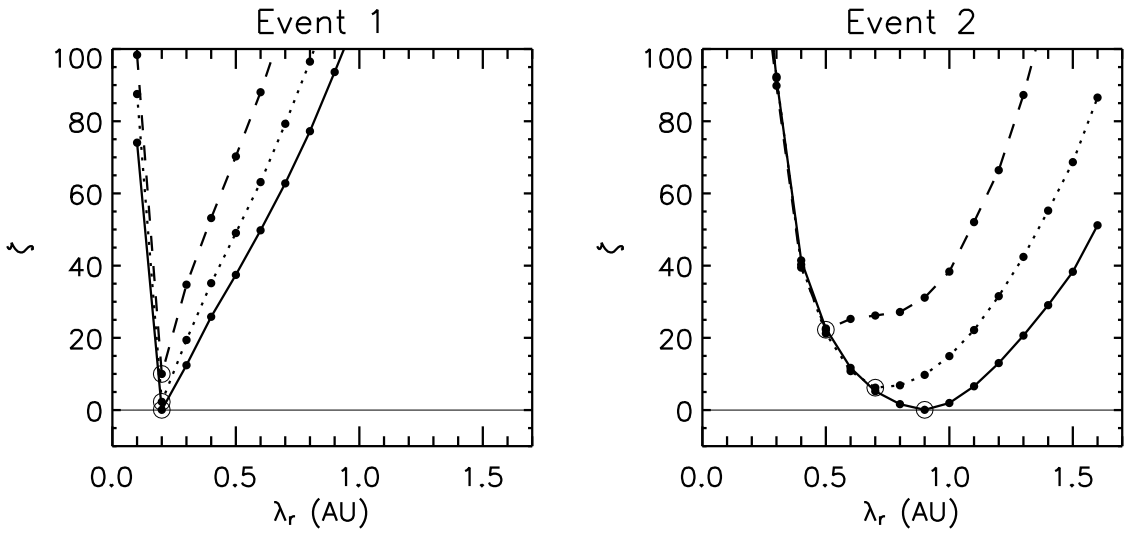

Figure 4.15: Goodness of fit estimator, ζ, obtained from the deconvolution of Event 1 (left) and Event 2 (right), considering statistical errors in the intensity measurements (see text for details). Same presentation as in Figure 4.5.

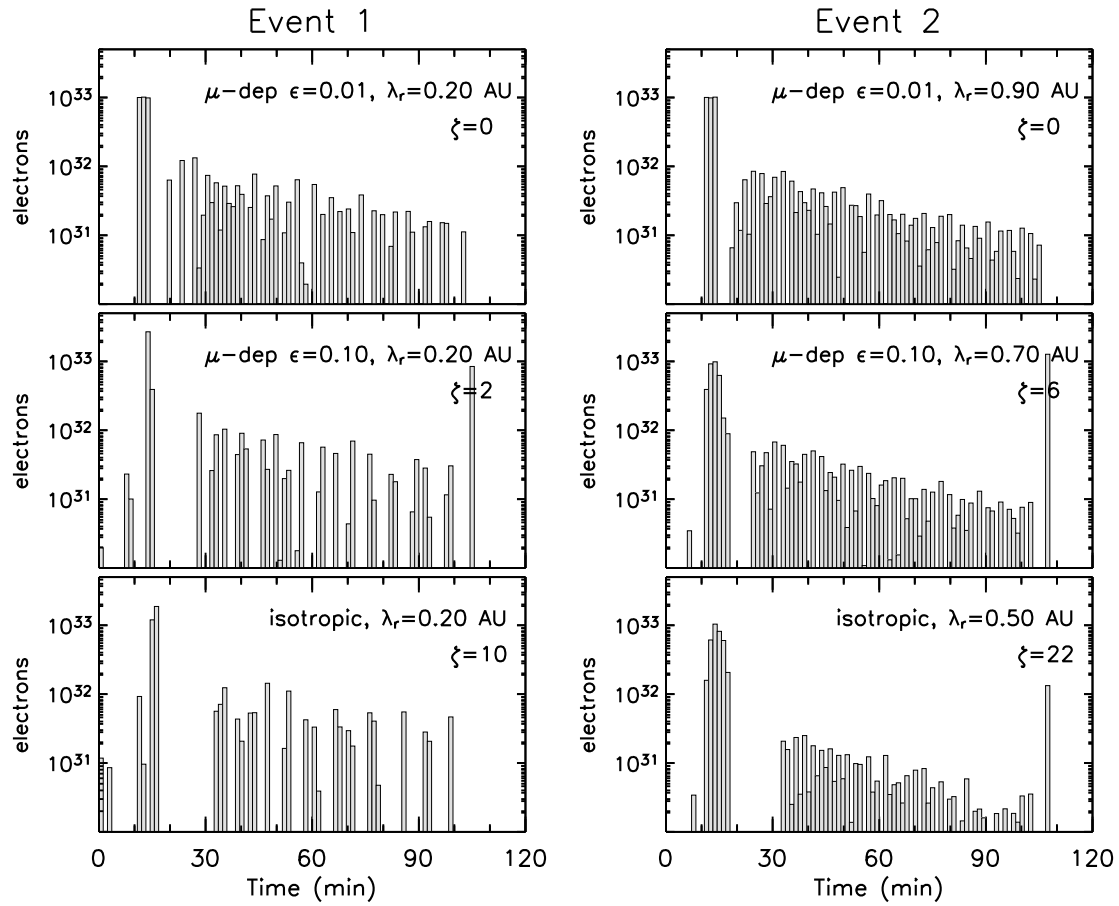

Figure 4.16: Best-fit electron injection profiles as a function of the scattering model for Event 1 (left) and Event 2 (right), considering statistical errors in the intensity measurements (see text for details). Same presentation as in Figure 4.7.

the magnetic field data that contains the error.

Figure 4.17 shows the values of ζ obtained from the deconvolution of Event 1 and Event 2, assuming magnetic field configuration (5) but adding a systematic offset of 0.05 nT in the B_z component. The obtained $\zeta(\lambda_r)$ profile is very similar if the offset is added in the x or y magnetic field component.

The values of $\zeta(\lambda_r)$ obtained for both events are quite similar to those obtained for configuration (5) in section 4.2.2 (see Figure 4.14), without taking into account the uncertainties in the magnetic field direction.

The lowest ζ value, $\zeta = 0$, is obtained for μ-dependent scattering with $\epsilon = 0.01$ and $\lambda_r = 0.2$ AU for Event 1, and $\lambda_r = 0.9$ AU for Event 2. In these two cases, the injection profile obtained from the deconvolution shows (i) an early prompt injection, and (ii) intermittency in the time-extended injection component (see upper panels in Figure 4.18). We therefore conclude that the deconvolution algorithm tries to cope with uncertainties in the magnetic field direction by decreasing and increasing the injection. The smaller the mean free path, the stronger the effect.

If we were to assume isotropic or μ-dependent scattering with $\epsilon = 0.10$, the best fit would correspond to $\lambda_r = 0.2$ AU for Event 1. In these two cases, the two injection episodes could be resolved (injection profiles are shown in the two left lower panels of Figure 4.18) but, (i) the onset of the first prompt injection would be blurred by previous weaker injection episodes, (ii) the onset of the second injection episode would be delayed, and (iii) its decay phase would show noticeable intermittency. For Event 2, the best fit would correspond to $\lambda_r = 0.5$ AU for isotropic scattering and $\lambda_r = 0.7$ AU for μ-dependent scattering with $\epsilon = 0.10$. Thus, if we did not know that the actual scattering processes are described by μ-dependent scattering with $\epsilon = 0.01$, we would underestimate the value of λ_r. The two injection episodes could be resolved (see two lower right panels of Figure 4.16) but they would show the same characteristics as discussed for Event 1; points from (i) to (iii).

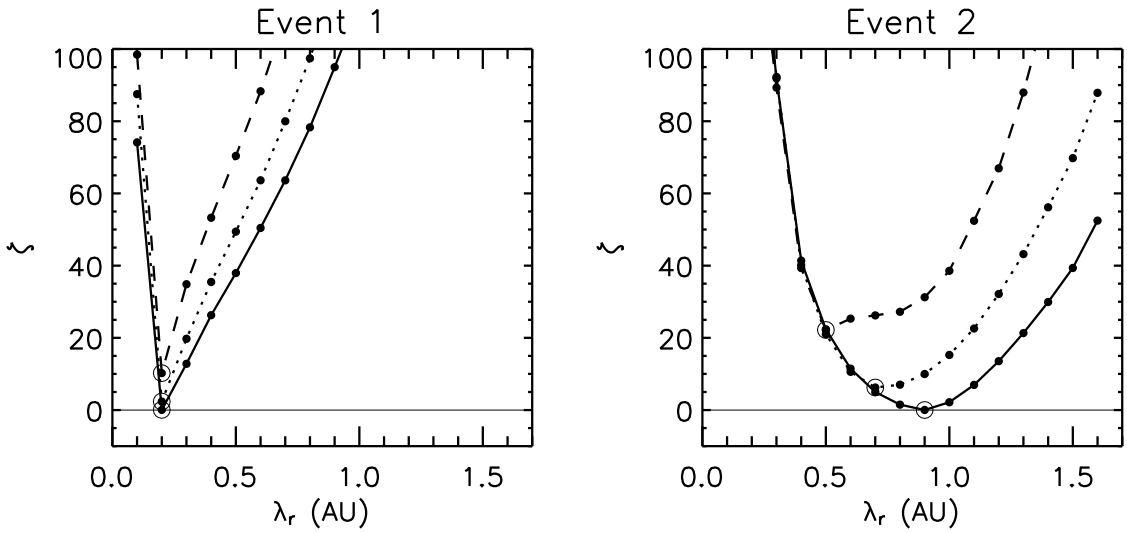

Figure 4.17: Goodness of fit estimator, ζ, obtained from the deconvolution of Event 1 (left) and Event 2 (right) considering an offset of 0.05 nT in the measurement of B_z (see text for details). Same presentation as in Figure 4.5.

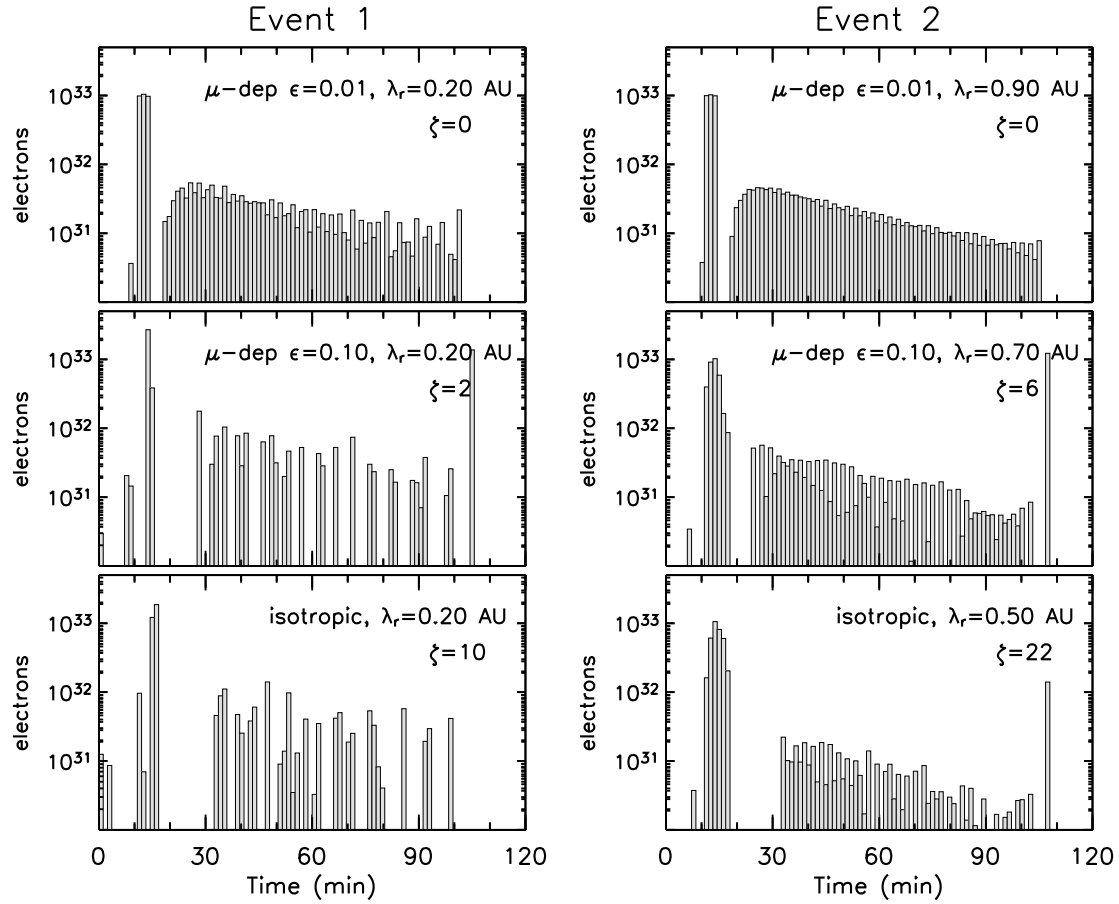

Figure 4.18: Best-fit electron injection profiles as a function of the scattering model for Event 1 (left) and Event 2 (right) considering a systematic 0.05 nT offset in the measurement of B_z (see text for details). Same presentation as in Figure 4.7.